

A High-Torque Low-Speed Multiphase Brushless Machine—A Perspective Application for Electric Vehicles

Marcelo Godoy Simões, *Senior Member, IEEE*, and Petronio Vieira, Jr., *Associate Member, IEEE*

Abstract—This paper presents the design, analysis, simulation, and modeling of a high-torque low-speed multiphase permanent-magnet brushless machine. The machine fits an in-wheel motor arrangement to be used for electric vehicle applications. This paper presents issues regarding the high-level modeling comprised of a transient model in conjunction with their corresponding experimental evaluation. Analysis was made to combine the modeling efforts with the expected behavior concerned with mutual inductance and armature reaction effects, so as to have realistic simulation results verified by the experimental setup. Comprehensive experimental results corroborate the work.

Index Terms—Brushless machines, digital signal processors, electric machines, modeling, motor drives.

I. INTRODUCTION

ELECTRIC vehicle (EV) propulsion systems have been historically driven by two distinct threads, because there are basically two ways to achieve high power density and high-efficiency drives. The first way is to employ high-speed motors, so that motor volume and weight will then be greatly reduced at the same rated output power. However, mechanical losses are incurred by the clutch, reduction, and differential gear during power transmission from the motor to the wheels. Increasing the motor speed may reduce the size and weight of the electric motor, but the corresponding values for the mechanical gearbox are likely to grow. The second thread for propulsion is to employ high-torque low-speed motors, which can directly drive the wheels [1], [2]. One standard solution is to connect a machine outside the hub so as to avoid unsprung mass effects on the suspension system. A high-torque low-speed in-wheel motor may be implemented in several topologies, but permanent-magnet brushless (PMB) machines are preferable due to the higher efficiency.

This paper describes the design of a PMB direct-driven wheel motor drive system comprising a multiphase multipole topology controller. It presents the high-level modeling, where a general dynamic model for a multiphase PMB, in conjunction with the corresponding inverter, is used to simulate the system. Experimentation and static evaluation were sought to fully complement the equation parameters.

Manuscript received December 14, 2000; revised May 9, 2002. Abstract published on the Internet July 15, 2002.

M. G. Simões is with the Engineering Division, Colorado School of Mines, Golden, CO 80401-1887 USA.

P. Vieira, Jr., is with the the Computer and Electrical Engineering Department, Universidade Federal do Pará, 66075-900 Belém, Brazil.

Publisher Item Identifier 10.1109/TIE.2002.803241.



(a)



(b)

Fig. 1. Multiphase brushless machine. (a) Rotor. (b) Stator.

II. MOTOR DESCRIPTION AND SPECIFICATIONS

Fig. 1 depicts a radial-flux-based motor. There are some advantages in radial flux motors [3]. One is a higher field intensity across the stator windings due to a better magnetic path. Another is utilization of standard rectangular magnets that are easier to handle (arc-shaped rare-earth magnets are difficult to make). Great progress regarding available energy density has been achieved with the development of rare-earth PMs; the latest grades of NdFeB have good thermal stability, enabling an increase in working temperature up to 100°C, larger coercivity, and corrosion resistance due to its coating protection.

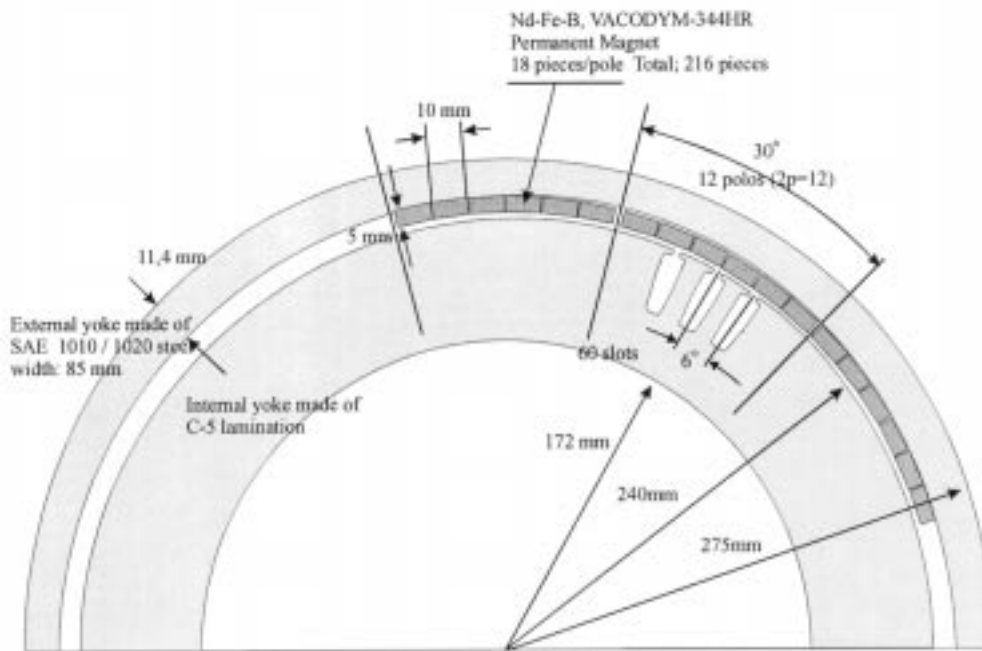


Fig. 2. Cutaway view across the machine.

Several advantages of high-phase drives have already been reported in the literature [4]–[6], such as: reduction of amplitude of pulsating torque and increased pulsating frequency easily filtered out by high-inertia applications; reduction of rotor harmonic currents; reduction of current per phase for the same rated voltage; and lowering the dc-link current harmonics. Higher reliability is also a very important characteristic of multiple-phase drives [7]. A high number of phases increases the torque-per-ampere ratio for the same machine volume. A multiphase drive is likely to be limited to specialized applications where high reliability is demanded such as in EV, hybrid EV, aerospace, ship propulsion, and high-power applications in which the requirements are not cost oppressive when compared to the overall system. Even though a higher number of phases would yield a smaller magnetic yoke and decreased volume and weight, the number of poles is restricted physically to the PM area and the rotor diameter [8]. A high number of poles is required in the design of a high-torque low-speed machine. Several tradeoff fundamental electromagnetic design studies were considered before the construction of the present machine, which ended up having ten poles and five phases. Sizing and power density issues depend on very complex relationships [4], [5]. In general, if stator leakage inductance and resistance are neglected, the output power for any machine can be expressed as

$$P_O = \eta \frac{m}{T} \int_0^T e(t) i(t) dt = \eta m K_p E_{pk} I_{pk} \quad (1)$$

where m is the phase number, and the EMF $e(t)$ and E_{pk} are the phase air-gap electromotive force (EMF) and its peak value, $i(t)$ and I_{pk} are the phase current and its peak phase current, T is the period of one cycle of the EMF, and the factor K_p is the electrical power waveform factor. Equation (1) shows that

a higher number of phases allows higher power density; the rationale for choosing a five-phase motor for this application has been presented in [9] and [10].

Fig. 1(a) shows the rotor, an external yoke made of SAE 1010 steel with a 275-mm external diameter with magnets bonded on the internal surface. Each pole has dimensions of $60 \times 80 \times 5$ mm. Fig. 1(b) shows the stator. The lamination was made with C-5 coating fully processed steel with 1.58 W/lb losses. The core lams were welded and the lamination package was cut with a CNC wire-electro-erosion machine. Since each coil of the winding must link the flux of one pole, 60 total slots, with 12 coils for each phase, were used to accommodate the five phases along the rotor perimeter. Therefore, for each pole, there are five slots to hold the windings (a higher number of slots would decrease the wire gauge leading to smaller rated current and torque). Each slot has two coils in a double-layer lap-winding construction. Fig. 2 outlines a cutaway view across the machine, indicating that each pole is constituted by three rows of six magnets (18 magnets/pole). The poles are made of a total of 216 NdFeB *Vacodyn 344 HR* magnets with high remanence (1.1 T) and coercivity (1275 kA/m).

The air gap (1.5 mm) has uniform flux distribution with small leakage between poles. Just as in any machine, the interaction between the flux imposed by the PM, and the magnetic flux dictated by the stator coils, creates the shaft torque. With a shaft-position optical sensor, the motor phase windings are excited sequentially to produce the desired torque and speed. The optical position system addresses to a lookup table, and the phase of this table is 90 electrical degrees apart at the beginning of the pair of poles. One winding is turned on at the same time that the next, which is just leaving the polar section, is turned off. Fig. 3 illustrates the timing of the motor phases, depicting the trapezoidal back EMF due to the PM flux and the currents that must be commanded by the position sensor (ideally, in phase

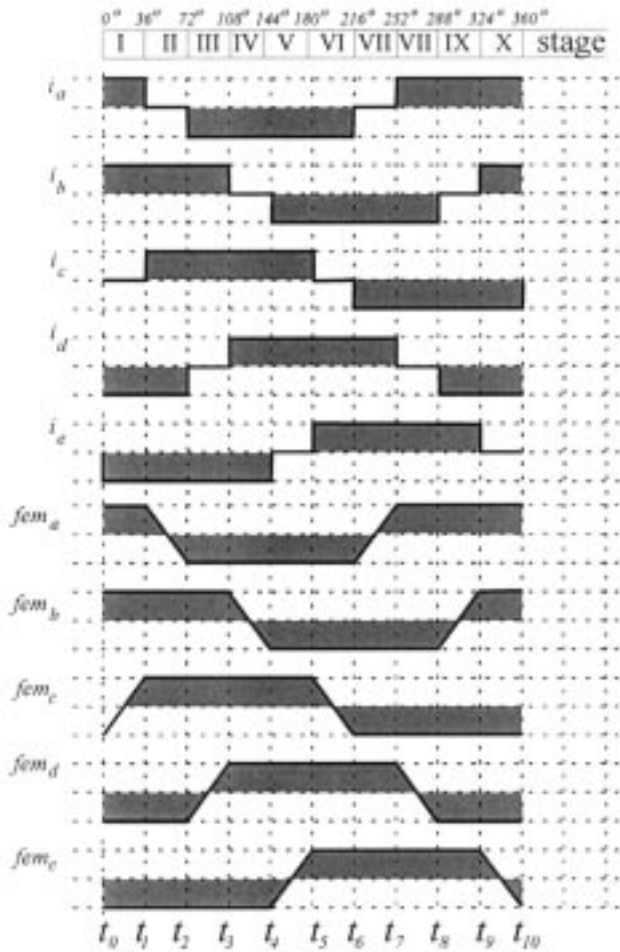


Fig. 3. Ideal machine excitation showing currents and back-EMF waveforms.

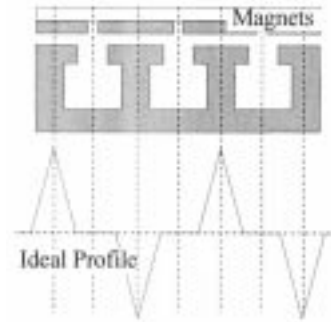
TABLE I
MOTOR PARAMETERS

External diameter: 275 mm
Axial length: 130 mm
Power rating: 3.2 HP
Poles: 12
Phases: 5
Nominal voltage: 140 V
Nominal current: 7.5 A
Rated speed: 750 RPM
Rated torque: 30 Nm

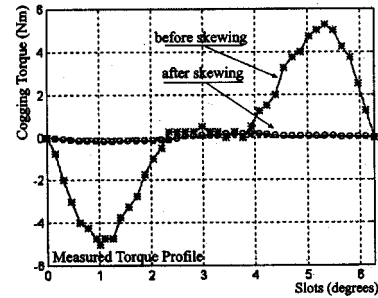
with the back-EMF voltages). Table I presents the nominal parameters for the present machine.

III. MODELING DEVELOPMENT

Section II emphasized that the primary use for the present motor is in high-bandwidth systems (in-wheel motor for traction, intelligent steering, adaptive cruise control, and intelligent transportation systems). Therefore, a preeminent model must be developed for the present machine, which can help to develop advance control strategies. In order to develop a useful dynamic model, the first concern was to eliminate the saliency (cogging) torque in this motor. Torque is generated by two distinct mechanisms. If self-inductance changes as a function of position,



(a)



(b)

Fig. 4. Cogging torque. (a) Theoretical torque profile before skewing. (b) Experimental evaluation before and after skewing.

reluctance torque is generated; if mutual inductance changes as a function of position, mutual or alignment torque is generated. The most common parasitic torque developed is called cogging torque, which is due to slotting on the stator. Cogging torque is the primary ripple component in the torque generated by a motor. In addition to cogging, there are a number of other sources of reluctance torque in a mutual torque motor, due to inevitable mechanical imperfections such as eccentricities and dimensional variations. Fig. 4(a) shows the cogging-torque distribution due to the interaction between the rotor magnets and the stator saliency with peak value proportional to the square of the air-gap flux; it increases and decreases linearly with the variation of the air-gap reluctance with the electrical angle. Fig. 4(b) compares the experimental cogging torque with flat slots against the cogging torque with skewed slots (very small). Skewing attempts to reduce cogging torque by making the derivative of the reluctance zero over each magnet face. The primary penalty of skewing is that it reduces the total flux linked to the stator winding and, consequently, the rated power. The clear advantage is that our modeling and control efforts will not need to deal with such effects. As a result, the mathematical modeling of the motor will be concerned only with lumped electromagnetic and circuits issues.

A power circuit inverter for a PM brushless machine requires an absolute encoder self-synchronization. Consequently, the model of that machine should not be dissociated from the inverter, (which is usually not considered in the modeling of dc machines and induction machines). Fig. 5 shows how the five-phase power circuit inverter is used and indicates the resistance drop, inductance, and back-EMF equivalent circuit, with a disconnected neutral point. By looking at Fig. 5, the state equations are easy to derive considering ten equivalent

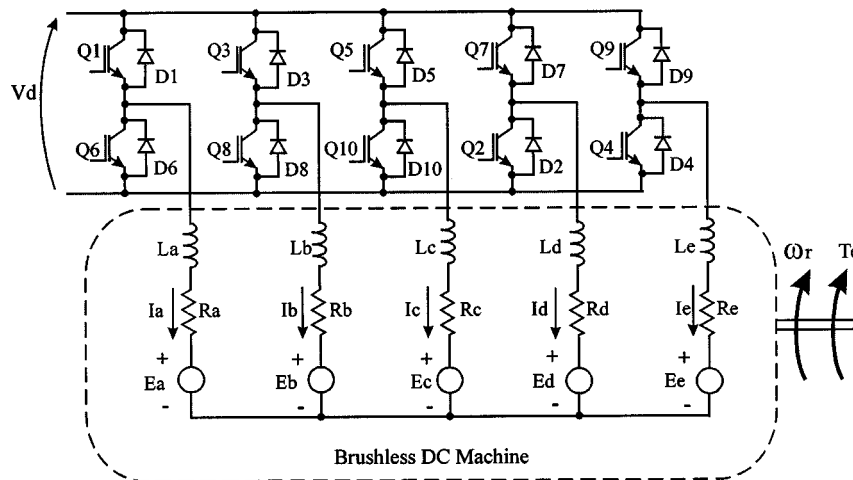


Fig. 5. Five-phase power circuit inverter.

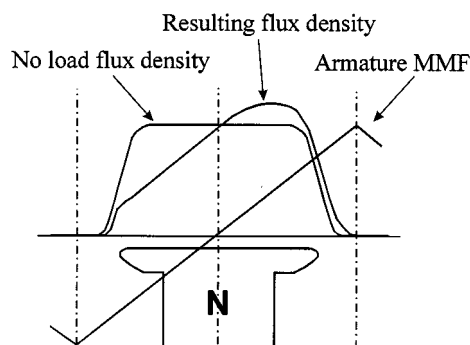


Fig. 6. Phenomenon of armature reaction along the polar face.

circuits occurring sequentially due the absolute position feedback command. Such equivalent circuits can be computed by considering which switches are imposing the bus voltage and which freewheeling diodes are conducting every 36 electrical degrees. Equation (2) shows the current flowing in phase A, during the first stage.

A complete model has ten equations, which are switched sequentially. Even though such a model has been extensively used in the literature [11]–[13], another issue was found to be very important for an accurate machine mathematical model: the mutual inductance between phases and the armature reaction [14]. Although such a phenomenon is usually neglected in high-power three-phase machines, considering that thickness of magnets plus air gap is too substantial, that is not actually the case for low-power machines [14], [15]. The stator currents impose a magnetomotive force (MMF) with a spatial triangular distribution while the magnets MMF distribution is essential triangular. Both superimpose along the air gap, initially increasing and then decreasing. The resulting MMF is indicated in Fig. 6. In the absence of saturation, the relation of flux and MMF is linear. However, as indicated in Fig. 6, saturation occurring at the leading pole tip for the motoring mode (or

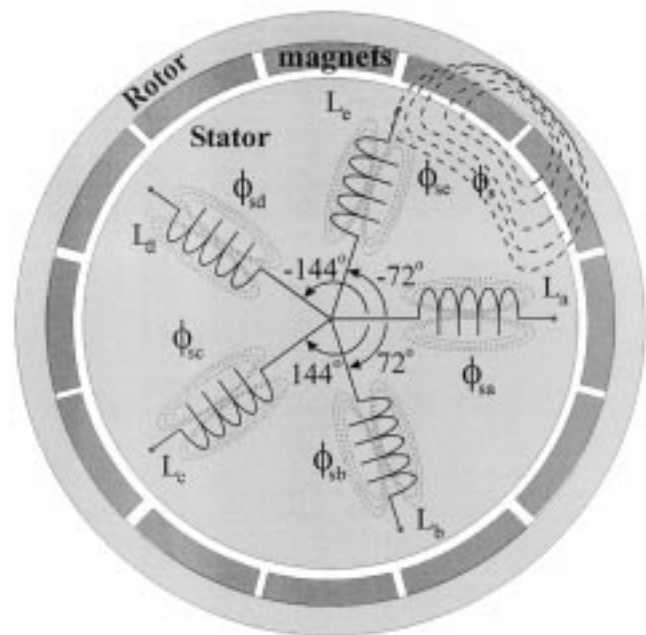


Fig. 7. Electromagnetic path across the air gap.

trailing pole tip for the regenerative mode) makes the increase in the flux density at the leading pole less than the flux-density reduction at the trailing pole which remains unsaturated. The net result is that the average flux density under the pole face is reduced, yielding a lowered output torque.

Considering the mutual inductance, one can observe, from Fig. 7, the equivalent electromagnetic paths in a more realistic electromagnetic circuit. The air-gap flux is composed of five contributions as indicated by (3). The inductance matrix is composed as indicated by (4). Experimental parameter identification of self- and mutual inductance were performed to obtain those numerical values. Time derivative of the PM air-gap linkage flux composes the trapezoidal back EMF, and the time derivative of

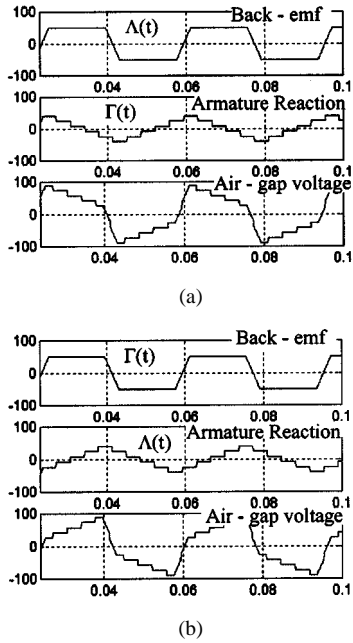


Fig. 8. Actual air-gap back-EMF composition. (a) Machine in motoring mode. (b) Machine in regenerating mode.

the stator winding air-gap linkage flux composes the effect of currents flowing through a self-inductance plus the mutual inductance (neglecting saturation and core losses) as shown in (5)

$$\frac{di_a}{dt} = \frac{1}{4L}(-4Ri_a - 3e_a + e_b + e_d + e_e + 2V_s - 4V_q) \quad (2)$$

where

- i_a phase-A current during first stage;
- L self-inductance of phase A;
- R winding resistance;
- e_a, e_b, e_d, e_e back EMF;
- V_q diode plus transistor voltage drop;
- V_s dc-link bus voltage.

Equation (4) indicates the natural choice of fluxes as state variables. There are two issues to make currents as a better decision [16]: 1) the inductance matrix ($[\lambda] = [L] \times [I]$) could be inverted and 2) there is one phase with null current every time. One can observe that, although the machine has five phases, every 36 electrical degrees there are only four phases conducting, while a fifth phase is kept off. For dynamic simulation, the inductance matrix must be numerically inverted each simulation step size. However, a Cholesky decomposition helped the matrix be expressed analytically and (6) permitted the dynamic simulation. The phase sequencing binds to the sequence defined by Fig. 3. Equations (3)–(5) show the general formulation for the five-phase machine. However, for each stage, there is one current kept to zero and the dimension of the dynamic system is consequently decreased to fourth order. Equation (6) shows such a reduced-order dynamical equation used in every stage of Fig. 3

$$\begin{bmatrix} \lambda_A \\ \lambda_B \\ \lambda_C \\ \lambda_D \\ \lambda_E \end{bmatrix} = \begin{bmatrix} \lambda_{ra} \\ \lambda_{rb} \\ \lambda_{rc} \\ \lambda_{rd} \\ \lambda_{re} \end{bmatrix} + \begin{bmatrix} \lambda_{sa} \\ \lambda_{sb} \\ \lambda_{sc} \\ \lambda_{sd} \\ \lambda_{se} \end{bmatrix} \quad (3)$$

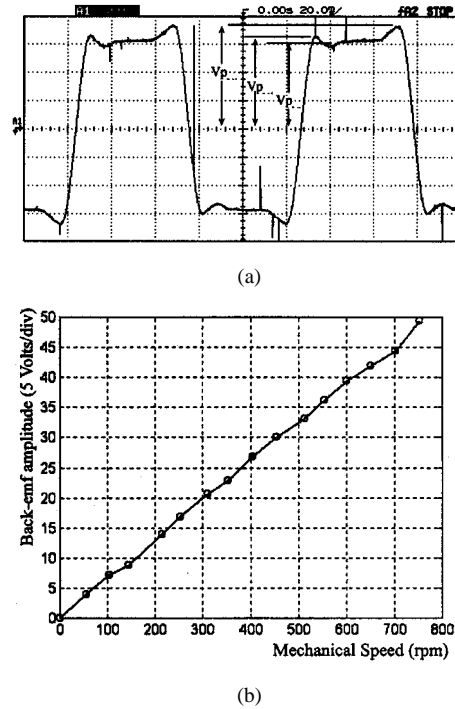


Fig. 9. Open-circuit assay. (a) Time response. (b) Speed constant determination (K_V).

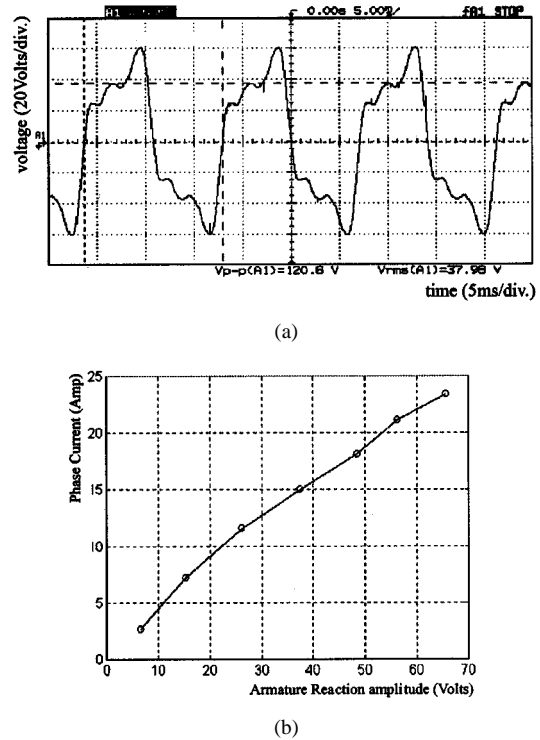


Fig. 10. Loaded-circuit assay. (a) Time response. (b) Current constant determination (K_A).

$$[V] = [R] \times [I] + \frac{d[\lambda]}{dt} \quad (4)$$

$$L = \begin{bmatrix} L_{aa} & L_{ab} & L_{ac} & L_{ad} & L_{ae} \\ L_{ba} & L_{bb} & L_{bc} & L_{bd} & L_{be} \\ L_{ca} & L_{cb} & L_{cc} & L_{cd} & L_{ce} \\ L_{da} & L_{db} & L_{dc} & L_{dd} & L_{de} \\ L_{ea} & L_{eb} & L_{ec} & L_{ed} & L_{ee} \end{bmatrix} \quad (5)$$

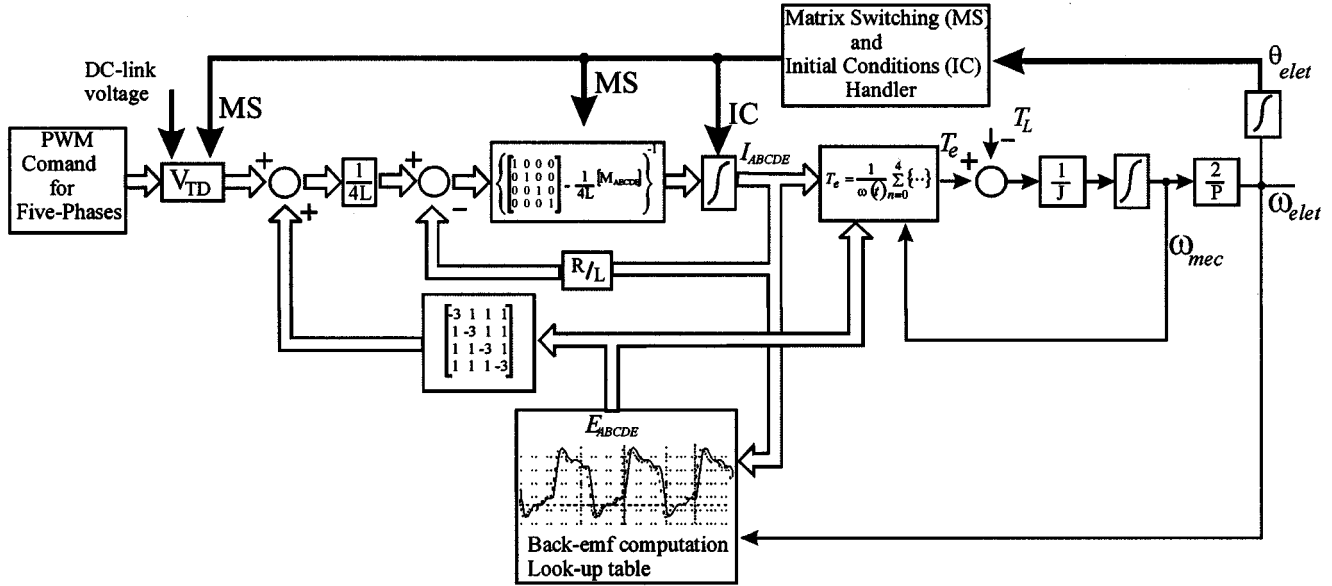


Fig. 11. Block diagram for transient simulation.

where

$[\lambda_{A,B,C,D,E}]$	total air-gap flux;
$[\lambda_{ra,rb,rc,rd,re}]$	PM air-gap linkage flux;
$[\lambda_{sa,sb,sc,sd,se}]$	stator windings air-gap linkage flux;
$[V]$	$= [V_A \ V_B \ V_C \ V_D \ V_E]^T$ phase volt-ages;
$[I]$	$= [I_A \ I_B \ I_C \ I_D \ I_E]^T$ phase cur-rents;
$[\lambda]$	$= [\lambda_A \ \lambda_B \ \lambda_C \ \lambda_D \ \lambda_E]^T$ total linked fluxes;
L_{ij}	inductance of phase i related to phase j ;

$$\frac{d}{dt} [I_{ABCDE}] = \left\{ \begin{bmatrix} 1 & 0 & 0 & 0 \\ 0 & 1 & 0 & 0 \\ 0 & 0 & 1 & 0 \\ 0 & 0 & 0 & 1 \end{bmatrix} - \frac{1}{4L} [M_{ABCDE}] \right\}^{-1} \cdot \frac{1}{4L} \left\{ -4R [I_{ABCDE}] + \begin{bmatrix} -3 & 1 & 1 & 1 \\ 1 & -3 & 1 & 1 \\ 1 & 1 & -3 & 1 \\ 1 & 1 & 1 & -3 \end{bmatrix} \times [E_{ABCDE}] + [V_{TD}] \right\} \quad (6)$$

where

$[I_{ABCDE}]$	current matrix for the stage;
$[E_{ABCDE}]$	back EMF for the stage;
$[M_{ABCDE}]$	mutual inductance matrix for the stage;
$[V_{TD}]$	matrix for dc link, transistor, and diode volt-ages.

Because the poles are not salient, the flux is homogenous along the air gap and the inversion is required just once [16]. Therefore, the same fourth-order system is equivalent every 36

electrical degrees, as long as the equations have their variables redefined in accordance with the currents that are flowing, and the four integrator initial conditions are introduced from the previous stage, (i.e., each stage has its own current matrix, back-EMF matrix, mutual matrix, transistor, and diode drop matrix). The armature reaction is fundamentally necessary to have a more realistic system response. Fig. 8 shows how the actual air-gap back EMF is composed by the addition of a trapezoidal normalized function due the PM-induced motional voltage (Γ_ω) added to a triangular normalized function for the armature reaction voltage (Λ_c). Therefore, two experimental evaluations for back EMF were required: 1) open-circuit back EMF in the whole speed operating range and 2) fully loaded machine to obtain the armature reaction. The five-phase PMB was rotated like a generator in open circuit. In order to load the machine to observe the armature reaction effects, resistive loads were connected in star and the BPM was operated as a generator with an auxiliary dc machine rotating the shaft. Fig. 9 shows the trapezoidal back-EMF waveform for such conditions. A lookup table was made to emulate such response, and Fig. 9(b) shows the experimental measurement of the constant K_v . The trapezoidal waveform was, by its turn, distorted like Fig. 10, the amplitude of such distortion was proportional to the current, as depicted in Fig. 10(b) by the constant K_a , obtained experimentally.

A torque equation is required to complete the model. Under the energy modeling point of view the induced voltage by the changing electromagnetic stored energy (back EMF) delivers mechanical energy. Thus, the torque for the five phases BPM machine has to account the air-gap flux distortion by the armature reaction as shown in (7)

$$T_e = \frac{1}{\omega(t)} \sum_{n=0}^4 \left\{ \left(K_v |\omega(t)| \Gamma_\omega \left(t - \frac{n}{5} 2\pi \right) + K_a |i_n(t)| \Lambda_c \left(t - \frac{n}{5} 2\pi \right) \right) i_n(t) \right\} \quad (7)$$

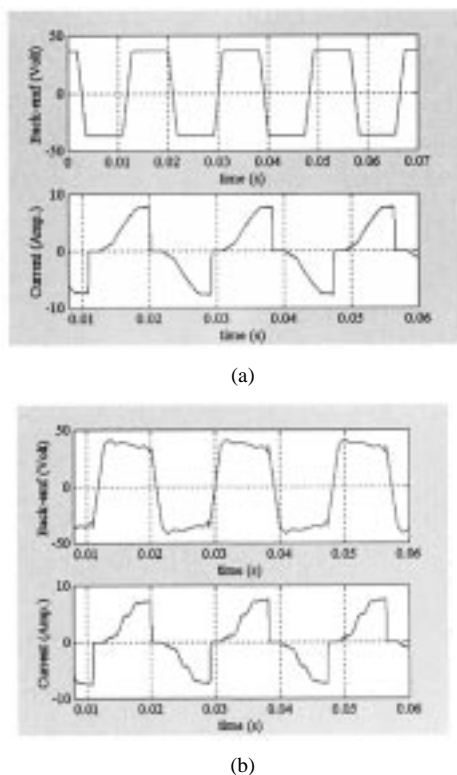


Fig. 14. Simulation results of back EMF and current for speed = 550 r/min. (a) Considering self and mutual inductances. (b) Considering armature reaction.

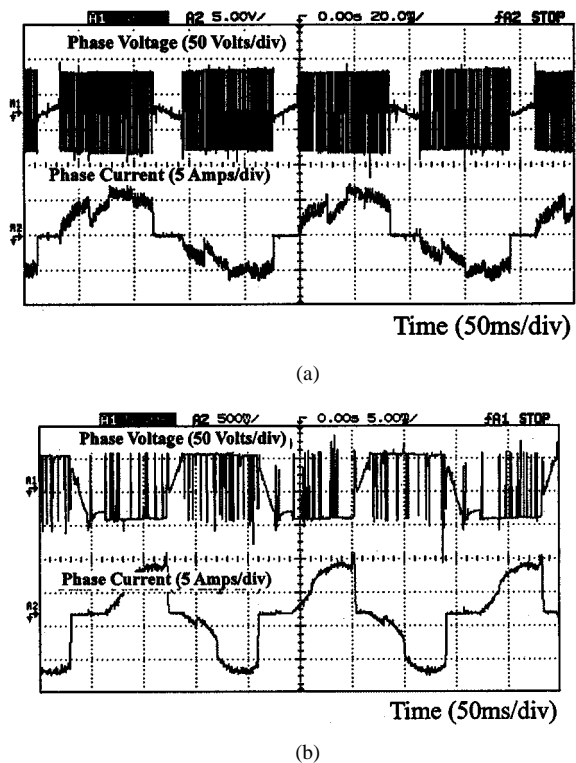


Fig. 15. experimental results. (a) Terminal voltage and current at load torque 40% of rated value. (b) Terminal voltage and current at load torque 80% of rated value.

only imposing an open-loop PWM scheme for the inverter. Fig. 13 presents the simulation results with the simplest model

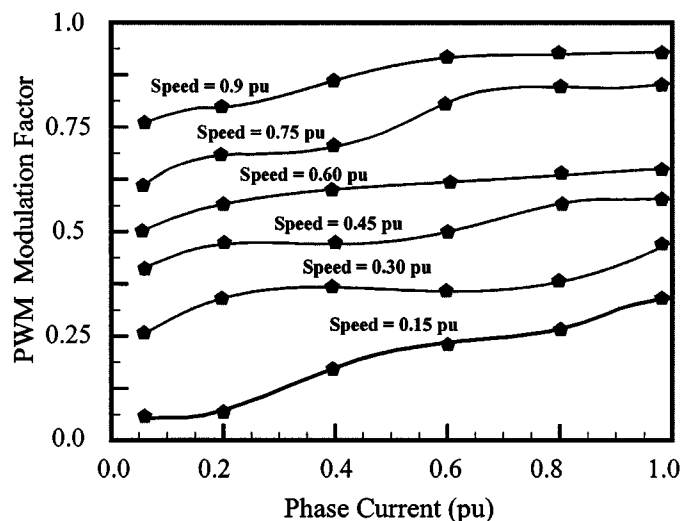


Fig. 16. Open-loop operating range.

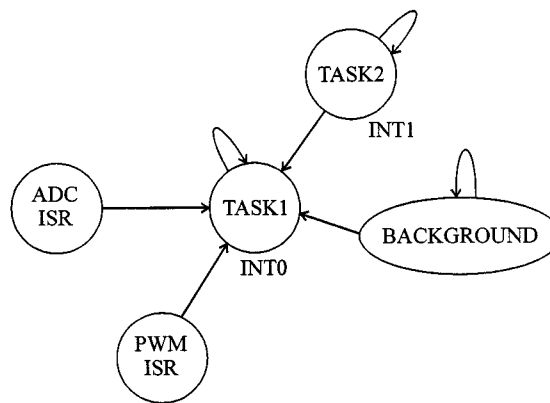


Fig. 17. Tasks coordination chart for the DSP control code.

based on the formulation of (2) where only the self-inductance and back EMF were taken into account for the machine. The current response is exponential with rise-time dictated by the long RL time constant and showing that, for high speed (550 r/min), there is no time for steady-state establishment. Even though such a model has been derived from the electrical equivalent circuit, the instantaneous actual current is much more complex. Therefore, the mutual-inductance-based model has been implemented based on the formulation of (3)–(7).

The incorporation of armature reaction in the model deforms the instantaneous back EMF. Fig. 14 shows the simulation results for such a model, Fig. 14(a) presents the effect of the mutual inductance, and Fig. 14(b) shows the armature reaction effect on the current waveform. Even though the currents are quite distorted, the experimental results depicted in Fig. 15 corroborate those simulation responses quite well. One can compare both figures to observe the current changing from a definite shape in low speed to a more complex rise time due to the armature reaction, followed by a spike and an abrupt fall time at the current trailing edge due to the armature reaction reduction on the back EMF. Fig. 15(a) shows the typical commutation torque

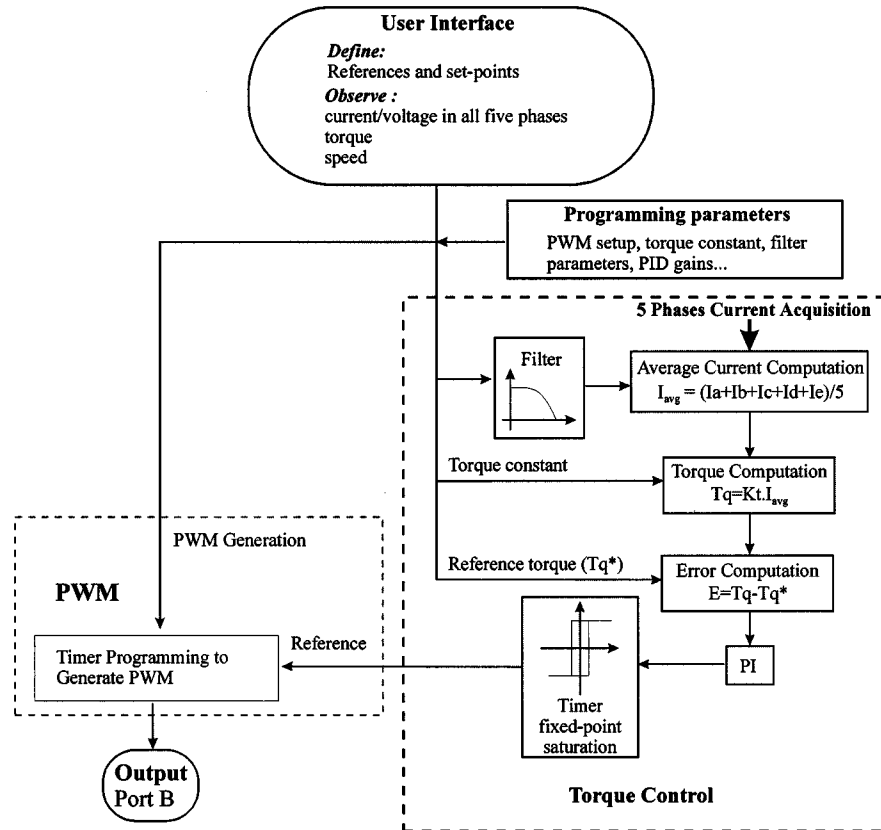


Fig. 18. Torque control implementation structure.

ripple for low load at the shaft, and Fig. 15(b) shows the distorted phase current due the effect of the armature reaction. It is important to observe that such a phenomenon shifts the position of the flux density distribution axis from the geometric interpolar axis, against the direction of rotation. Consequently, for high load at the shaft the commutation torque ripple is overcome by the armature reaction effect.

Fig. 16 shows a family of curves for the machine operating in open loop, depicting the current phase peak on the horizontal axis and the PWM duty cycle on the vertical axis for a range of rotor speed. Such a diagram is very important for the understanding of how the machine operates and how a closed-loop torque control will eventually act.

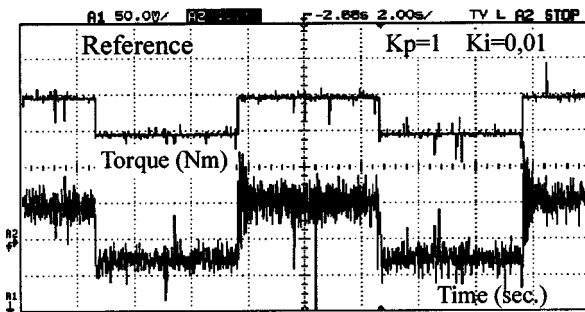
V. TORQUE CONTROL LOOP

A custom-made Motorola 56824-based DSP board was designed and implemented for this project. The description of such a board is outside the scope of this paper and is available in [17]. CodeWarrior user-friendly tools were used for software development and debugging. The board is plugged into a host personal computer running the tasks indicated in Fig. 17. A dual-access 64 K memory on the DSP board provides the background communication. Although the PC can read and write other memory areas on the board, it incurs more overhead because the DSP chip must be held during

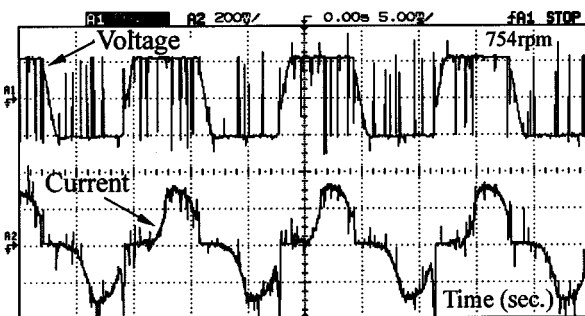
PC accesses. The variables or arrays that are being passed must be defined as global variables. These locations can hold pointers to variables or arrays of pointers; therefore, they are used to communicate between the processor boards and the PC. The control software that runs in the DSP-PC board is a multitasking real-time program. Therefore, it is necessary to trigger the interruptions by software in such a way that lower level interruptions can be interrupted by higher level ones with automatic context save/restoring of variables. The most critical time assignment task is the operation of the PWM timers and the ADC converters.

The eight-channel ADC conversion is triggered at the end of task 1. Although, the complete conversion of the four channels takes $32 \mu\text{s}$, which is inside the $100\text{-}\mu\text{s}$ setup for the PWM. The PWM is activated by two timers, one decrementing from an initial value and another one setting it up again to recount. For the Motorola DSP56824 internal clock setting, the duty-cycle resolution ranges from 100 ns to 13.1 ms. A semaphore handler coordinates Task #1 for acquisition and PWM setup while Task #2 runs at 1 ms, for the torque control loop which contains a first-order infinite-impulse response (IIR) filter for torque estimation plus a discrete proportional-integral (PI) controller. The timing is roomy enough for background communications within the control loop structure indicated in Fig. 18.

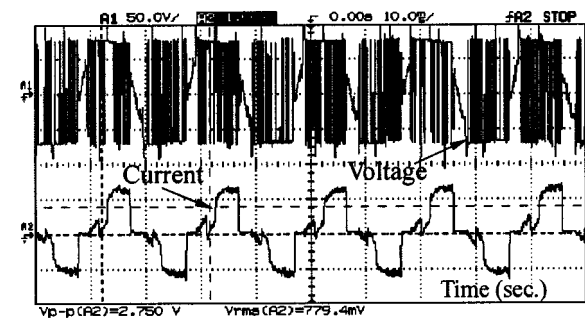
The control loop structure has four main routines: 1) input/output of analog data; 2) input/output of digital data



(a)



(b)



(c)

Fig. 19. Torque control. (a) Step response. (b) Terminal voltage and current for low torque level. (c) Terminal voltage and current for high torque level.

(PWM five-phase output included); 3) signal filtering; and 4) torque control. The procedure is to acquire and filter the five phase currents, estimate the average value which is proportional to the instantaneous torque, estimate torque by using the experimental torque parameter, compute error with the reference, process a PI difference equation and, finally, program the PWM initialization with the PI result bounded to internal scaling. Fig. 19(a) shows a step torque response, from 5 to 15 N-m with corresponding terminal voltage and current for both conditions indicated in Fig. 19(b) and (c). The speed was kept within the range, from 650 to 750 r/min, with a dc machine connected to the shaft and shunt resistances absorbing the incoming power.

VI. CONCLUSION

This paper has presented the modeling evolution of a multi-phase high-torque low-speed PMB machine used as an in-wheel

EV propulsion scheme. Issues regarding a high-level modeling comprised a general dynamic model in conjunction with the corresponding experimental evaluation. Analysis was made to combine the modeling efforts with the expected behavior of mutual inductance and armature reaction effects, so as to have simulation results verified by the experimental results. The dynamic model was implemented with Simulink/MATLAB. A DSP-based torque loop control was implemented and tested, thus integrating the in-wheel machine with a dc machine acting as a load.

ACKNOWLEDGMENT

The authors are sincerely grateful for the technical guidance, help, and suggestions from Dr. I. E. Chabu and Dr. C. Goldemberg.

REFERENCES

- [1] D. Patterson, "Design and development of an axial flux permanent magnet brushless DC motor for wheel drive in a solar powered vehicle," *IEEE Trans. Ind. Applicat.*, vol. 31, pp. 1054–1061, Sept./Oct. 1995.
- [2] T. F. Chan and L.-T. Yan, "In-wheel permanent-magnet brushless dc motor drive for an electric bicycle," in *Proc. IEEE IEMDC'99*, May 1999, pp. 407–409.
- [3] G. H. Chen and K. J. Tseng, "Computer-aided design and analysis of direct-driven wheel motor drive," *IEEE Trans. Power Electron.*, vol. 12, pp. 517–527, May 1997.
- [4] D. Qin, R. Qu, and T. A. Lipo, "A novel electric machine employing torque magnification and flux concentration effects," in *Conf. Rec. IEEE-IAS Annu. Meeting*, vol. I, Oct. 1999, pp. 132–141.
- [5] S. Huang and T. A. Lipo, "Analysis and evaluation of the transverse flux circumferential current machine," in *Conf. Rec. IEEE-IAS Annu. Meeting*, vol. I, Oct. 1997, pp. 378–384.
- [6] P. Vieira Jr and M. G. Simões, "Development of a penta-phase brushless dc hub-motor," in *Proc. COBEP'98*, 1998, pp. 635–639.
- [7] S. Waikar, T. Gopalarathnam, H. A. Toliyat, and J. C. Moreira, "Evaluation of multiphase brushless permanent magnet (BPM) motors using finite element method (FEM) and experiments," in *Proc. IEEE APEC'99*, vol. I, 1999, pp. 396–402.
- [8] A. B. Proca, A. Keyhani, and A. EL-Antably, "Analytical model for permanent magnet motors with surface mounted magnets," in *Proc. IEEE IEMDC'99*, 1999, pp. 767–769.
- [9] M. G. Simões and P. Vieira Jr., "Model development and design of a wheel-motor drive system," in *Proc. EPE-PEMC*, vol. 5, Kosice, Slovak Republic, Sept. 5–7, 2000, pp. 74–79.
- [10] M. G. Simões, N. N. Franceschetti, and P. Vieira Jr., "Design and evaluation of a polyphase brushless DC-machine direct drive system," in *Conf. Rec. IEEE-IAS Annu. Meeting*, Chicago, IL, 2001, CD-ROM.
- [11] P. Pillay and R. Krishnan, "Modeling of permanent magnet motor drives," *IEEE Trans. Ind. Electron.*, vol. 35, pp. 537–541, Nov. 1988.
- [12] R. Spée and A. K. Wallace, "Performance characteristics of brushless dc drives," *IEEE Trans. Ind. Applicat.*, vol. 24, pp. 568–573, July/Aug. 1988.
- [13] P. D. Evans and D. Brown, "Simulation of brushless dc drives," *Proc. Inst. Elect. Eng.*, vol. 137, pp. 299–308, Sept. 1990.
- [14] C. Goldemberg and O. S. Lobosco, "Modeling of a PM converter-fed machine allowing for armature reaction and damper cage effects," in *Proc. ICEM'96*, vol. 3, Vigo, Spain, Sept. 10–12, 1996, pp. 85–90.
- [15] O. S. Lobosco, "Modeling and simulation of dc motors in dynamic conditions allowing for the armature reaction," *IEEE Trans. Energy Conversion*, vol. 14, pp. 1288–1293, Dec. 1999.
- [16] C. Goldemberg and A. A. Penteado Jr., "Induction motor transient analysis in the ABC/abc reference frame," in *Proc. Electrimacs'99*, vol. III, Lisbon, Portugal, Sept. 14–16, 1999, pp. 153–158.
- [17] S. Szaifir and M. G. Simões, "Real time electrical motor control using DSP based system," in *Proc. IEEE INDUSCON 2000*, vol. 1, Porto Alegre, Brazil, Nov. 6–9, 2000, pp. 59–64.



Marcelo Godoy Simões (S'89–M'95–SM'98) received the B.S. and M.Sc. degrees in electrical engineering from the University of Sao Paulo, Sao Paulo, Brazil, in 1985 and 1990, respectively, the Ph.D. degree in electrical engineering from the University of Tennessee, Knoxville, in 1995, and the Livre-Docencia (D.Sc.) degree in mechanical engineering from the University of Sao Paulo, in 1998.

He is currently an Associate Professor at the Colorado School of Mines, Golden, where he is working to establish several research and education activities. His interests are in the research and development of intelligent applications, fuzzy logic and neural networks applications to industrial systems, power electronics, drives, machine control, and distributed generation systems.

Dr. Simões is a recipient of a National Science Foundation (NSF)—Faculty Early Career Development (CAREER) Award, which is the NSF's most prestigious award for new faculty members, recognizing activities of teacher/scholars who are considered most likely to become the academic leaders of the 21st century.



Petronio Vieira, Jr. (S'98–A'01) received the B.S. degree in electrical engineering from the Federal University of Pará, Belém, Brazil, in 1985, the M.Sc. degree in power electronics from the Federal University of Santa Catarina, Florianópolis, Brazil, in 1996, and the Ph.D. degree in mechatronics from the University of Sao Paulo, Sao Paulo, Brazil, in 2000.

He was a Visiting Research Fellow at the Colorado School of Mines, Golden, in 2000. He was with the "Centrais Elétricas do Norte do Brasil S.A." during 1985–1987, working on the maintenance of synchronous 300-MW generators. Since 1987, he has been with the Computer and Electrical Engineering Department (DEEC), Federal University of Para, where he has been involved in teaching undergraduate courses on energy conversion and power electronics and graduate courses on electronic drives. He is the coordinator of the Power Electronics Laboratory in the DEEC. His main research interests are control, instrumentation, and electronic drives for industrial applications and systems.

Dr. Vieira is member of the Brazilian Power Electronics Society (SOBRAEP) and Brazilian Society of Maintenance (ABRAMAN).